


Laser Clad and HVOF-Sprayed Stellite 6 Coating in Chlorine-Rich Environment with KCl at 700 °C

Zdenek Pala¹ · Mingwen Bai¹ · Frantisek Lukac² ·
Tanvir Hussain¹ 

Received: 25 August 2016 / Revised: 13 February 2017 / Published online: 20 April 2017
© The Author(s) 2017. This article is an open access publication

Abstract Laser clads and HVOF coatings from a stellite 6 alloy (Co–Cr–W–C alloy) on 304 stainless steel substrates were exposed both bare and with KCl deposits in 500 ppm HCl with 5% O₂ for 250 h at 700 °C. SEM/EDX and PXRD analyses with Rietveld refinement were used for assessment of the attack and for analysis of the scales. The bare samples suffered from scale spallation and the scale was mostly composed of Cr₂O₃, CoCr₂O₄ and CoO, although due to dilution haematite (Fe₂O₃) was detected in the scale formed on the laser clad sample. A small amount of hydrated HCl was detected in bare samples. While the corrosion of the bare surfaces was limited to comparatively shallow depths and manifested by η and M₇C₃ carbide formation, the presence of KCl on the surface led to severe Cr depletion from the HVOF coating (to 1 wt%). Both inward and outward diffusion of elements occurred in the HVOF coating resulting in Kirkendall voids at the coating–steel interface. The laser clad sample performed significantly better in conditions of the KCl-deposit-induced corrosion. In addition to the oxides, CoCl₂ was detected in the HVOF sample and K₃CrO₄ was detected in the laser clad sample. Thermodynamic calculations and kinetic simulations were carried out to interpret the oxidation and diffusion behaviours of coatings.

Keywords Stellite 6 · KCl · High-temperature corrosion · HVOF · Laser cladding

✉ Tanvir Hussain
tanvir.hussain@nottingham.ac.uk

¹ Faculty of Engineering, University of Nottingham, University Park, Nottingham NG7 2RD, UK

² Institute of Plasma Physics CAS, Za Slovankou 3, Prague, Czech Republic

Introduction

Cobalt–chromium–tungsten–carbon-based stellite quaternary alloys have long been established as a high-temperature wear resistant material [1]. This is owing to the facts that both of its allotropic modifications: face-centred cubic (fcc) and hexagonal closed-packed (hcp) are of close-packed type and to the sluggishness [2] in the fcc-to-hcp transformation that commonly leads to coexistence of both structures in the surface layers. The close-packed arrangement of atoms has profound consequences on mechanical properties due to the mechanism of plastic flow by slip (p. 40, 336 in [3]) which, together with strain-induced fcc-to-hcp transformation, govern the wear resistance. Alloying with chromium is vital from wear, corrosion and oxidation viewpoints; as a carbide former, the presence of chromium can contribute to the precipitation of M_7C_3 , which along with η carbide is the most common carbide in stellite alloys. At the same time, chromium adds strength and improves corrosion and oxidation resistance when solid-solutioned in the matrix [4]. The amount of chromium is usually dictated by the targeted exposure environment. For example, when erosion–corrosion is envisaged, the chromium level is greater than 25 wt% [5]. Because of deterioration in erosion–corrosion properties of molybdenum-containing alloys [5], molybdenum is being substituted by tungsten which acts mainly as a strengthener to the matrix. Alloying with tungsten also leads to η carbide formation [6]. Eventually, the closed-packed structure makes the stellite alloys prone to the emergence of stacking faults, or perturbations in the stacking sequence, which originate via mechanical and/or thermal treatment routes (p. 65 in [7]) both of which are present during thermal spraying and laser cladding. Even though stacking faults were reported to enhance the wear resistance of cobalt base alloys [8], it is not a universally accepted opinion. Moreover, the presence of stacking faults bears even more significance for the coatings and clads which have been reported several times as carbide-free [9] in stark contrast to both cast and wrought stellites.

A decade ago in a comprehensive study by Hjörnhede et al. [10], a laser clad stellite 6 (750 μm thick) and an arc sprayed Euronics 508 (460 μm), both Co–Cr–W–C type materials, were identified as the best performers in the demanding erosion–corrosion environment of both circulating and pressurized fluidized bed coal and biomass burning boilers in Sweden. At the same time, high velocity oxy-fuel (HVOF) sprayed stellite 6 coating (300 μm thick) was reported [11] as having better hot corrosion resistance in coal-burning environment which was attributed to the formation of thick and continuous protective scales composed of spinel CoCr_2O_4 on top of CoO and Cr_2O_3 . In another study [12], HVOF-sprayed stellite 6 coating in molten salts exhibited beneficial effects of inter-splat oxides on corrosion propagation into the coating at 525 °C.

Oxidation of Co–Cr alloys lead to creation of a two-layered oxide scale with appreciable porosity [13]. While the pores enhance oxidation, the Cr_2O_3 and spinel CoCr_2O_4 phases inhibit the oxidation and the CoO serves as the phase through which the Co ions diffuse [14]. The oxidation is, however, strongly dependent not only on oxygen pressure, but mainly on the amount of chromium in the alloy. Alloys with more

than 25 wt% Cr have been reported to have both almost pure Cr_2O_3 scales according to Phalnikar et al. [15] and being of two-layer structure containing continuous layers of Cr_2O_3 and spinel CoCr_2O_4 [13] when oxidized in atmosphere with oxygen pressure above 13 kPa. The compactness of the scales, which improves with increase in Cr, is responsible for improved oxidation resistance [13] even though the overall spalling resistance was deemed as insufficient. However, in deposit-induced high-temperature corrosion environments with chloride species, Cr_2O_3 scale can be attacked by KCl deposits and K_2CrO_4 is formed which destroys the protective ability of the alloy and coating [16, 17]. In addition, several other authors have mentioned formation of volatile CrCl_2 in chromia-forming alloys using mechanism termed *active oxidation* [18]. There exists a gap in literature on the understanding of the behaviour of Co–Cr–W–C coatings in chlorine-rich environments.

In this study, a stellite 6 feedstock powder was deposited via liquid fuelled HVOF thermal spray and a powder-based fibre laser cladding routes. The microstructures of the coating and cladding were examined in detail and the samples were exposed in a controlled environment, high-temperature corrosion test rigs containing 500 ppm HCl, 5% oxygen and bal. nitrogen for 250 h at 700 °C. The samples were exposed both bare, to study gas phase attack, and covered in KCl to simulate deposit-induced fireside corrosion. The exposure conditions were chosen to reflect the temperatures in the superheaters of the latest generation of steam generators operating under ultra-supercritical conditions with biomass as a fuel where metal temperatures will be in excess of 650 °C [19].

Experimental Procedures

Materials and Coatings Deposition

A stellite 6 powder with median diameter (D50) of 38 μm , as determined by Malvern Master Sizer (Malvern, UK), was used both for deposition of HVOF coating and laser clad on AISI 304 stainless steel substrates (nominal composition Fe-19.0Cr- 9.3 Ni-0.05 C wt%). The powder had nominal composition of Co-28.3Cr-4.8W-2.2Ni-1.5Fe-1.2Si-1.2C and quantitative Rietveld analysis (QRR) of powder X-ray diffraction (PXRD) data revealed a two-phase solid solution composition comprised of ~ 9 wt% hcp structure and ~ 91 wt% fcc. The absence of carbides in the powder and typical microstructure of the solid solution were determined from cross sections of particles in a scanning electron microscope (SEM).

Laser cladding was done by a 2 kW ytterbium doped fibre laser ($\lambda = 1070$ nm) by IPG Photonics (Burbach, Germany). The samples were degreased before the cladding. The substrate was 6 mm thick in order to withstand the significantly higher heat loads compared to thermal spraying. Pre-track cleaning and preheating of the substrate were performed at 0.5 kW laser power at the same scanning speed used for cladding deposition. All operations on the substrate were performed under a controlled environment in a chamber which was back-filled with argon. The powder was fed at 16 g/min under the angle of 28° and a 10 mm stand-off distance. Argon was used as a carrier gas. Optimized deposition conditions were as follows: 1.6 kW

laser power, 212 mm working distance, 20 mm defocus distance, spot size of 3.6 mm, fibre size 0.6 mm and a scanning speed of 600 mm/min. The optimization was performed by analysing 12 single track clads deposited under various conditions. The overlap in the deposited laser clad was 50%.

Metjet IV, a liquid fuel-based HVOF system by Metallisation Ltd. UK, was used for thermal spraying with kerosene as the fuel. The samples were grit blasted with brown alumina and ultrasonically cleaned before the coating deposition. The substrates were 1.5 mm thick, 60 mm long and 25 mm wide. The coatings were deposited within 8 passes resulting in uniform thickness of $\sim 250 \mu\text{m}$. The samples were air-cooled during spraying. The length of the nozzle of the HVOF gun was 100 mm, and a stand-off distance of 356 mm was used during the spray runs. The flow rates of kerosene and oxygen were 476 ml/min and 920 l/min, respectively, and nitrogen was used a carrier gas for the powder.

High-Temperature Controlled Environment Corrosion Tests

The coatings and clads were precision cut by a water jet with garnet abrasive into smaller sections of 10 mm by 10 mm. Since the effects of surface roughness were not of interest in this study, the coatings and clads surfaces were ground to P240 SiC finish and then were either left bare or covered with KCl deposit. A KCl suspension was prepared with ethanol, and the deposit was applied on the surface of the sample using a paint brush. The samples were dried before the test. A deposit flux of $\sim 0.3 \text{ mg/mm}^2$ for 250 h was applied only on the sample top surface. The samples were placed in individual alumina crucibles and exposed to a controlled environment, high-temperature corrosion test. The set-up contained a horizontal tube furnace with a stainless steel vessel and the inside of the chamber was entirely lined with high purity alumina. A mass flow controller was used to flow $35 \text{ cm}^3/\text{min}$ of gas composed of 500 ppm HCl/5% oxygen/bal. nitrogen through the chamber during the high-temperature corrosion test. The samples were heated and cooled under flowing nitrogen to avoid any corrosion at lower temperatures. The samples were exposed at $700 \text{ }^\circ\text{C}$ for a duration of 250 h. The samples with and without crucibles and deposits were weighted using a precision balance before and after the tests to track their progress.

Sample Characterization

After weighting, any loose deposits from the samples were collected and the corroded surfaces investigated in an FEI XL30 (FEI Europe, Eindhoven, The Netherlands) SEM operated at 20 kV in both secondary electron (SE) and backscattered electron (BSE) modes. The SEM was equipped with energy dispersive X-ray (EDX) detector that facilitated analysis of elemental compositions including area mapping. Powder X-ray diffraction (PXRD) measurements of the corroded surfaces were done in a Siemens D500 XRD system (Germany), a vertical θ - 2θ diffractometer in Bragg–Brentano set-up, using $\text{CuK}\alpha$ radiation and scintillation point detector with secondary monochromator. The scanned 2θ range was from 10° to 150° with 0.05° step size and 20 s of counting time in each step. Since some of the corroded products entirely spalled from the coating surface, the small

pieces were analysed by a vertical θ – θ diffractometer (Bruker AXS, Germany) in parallel beam geometry equipped with 1D LynxEye detector. Insertion of polycapillary optics and slit with diameter of 1 mm into the primary path of Fe β -filtered CoK α radiation allowed for pseudo-parallel beam that impinged on small spalled pieces. Due to small irradiated volume, a counting time of 384 s was used together with 0.035° step size in the range from 5 to 120° 2θ . Since the identification of crystalline phases only by using the *search match* mechanism embedded in standard software tools is often unambiguous, we employed Rietveld refinement [20] and checked the obtained values of refined lattice parameters in order to assess the viability of the identified phases. Since the irradiated volumes composed of phases in layers rather than isotropically distributed powder particles, the determined quantities have higher error. TOPAS software package (Bruker AXS, Germany) was employed for Rietveld analysis.

The exposed samples were cold-mounted using an EpoFix resin (Struers, Denmark) filled with glass beads to avoid shrinkage during curing, and the samples were sequentially ground and polished up to 1 μm diamond finish in a non-aqueous lubricant. The scales and the corrosion products were examined in a SEM with EDX elemental maps. All the presented images from the cross sections were made in the un-etched state and were done immediately after the final polishing step.

Thermodynamic Calculations and Kinetic Simulations

Thermodynamic calculation of oxide scale formation as a function of oxygen partial pressures at different temperatures was carried out by using the Thermo-Calc software (Version 2016b, Sweden) with the TCS Ni-based Superalloys Database (TCNi8). The composition of stellite 6 is set up according to Co–28.3Cr–4.8W–2.2Ni–1.5Fe, and the temperature is 700 °C. It is worth noting that all the calculations are based on thermodynamic data from the databases, which are produced by experts through critical assessment and systematic evaluation of experimental and theoretical data, following the well-established CALPHAD technique [21]. All calculations describe various phases in thermodynamic equilibria and follow the minimal Gibbs energy principle.

Diffusion module (DICTRA) was applied for accurate simulation of diffusion controlled reactions in multi-component alloy systems, which is based on numerical solution of the multi-component diffusion equations. In order to perform a diffusion simulation between stellite 6 coatings and 304 stainless steel at 700 °C (973 K) for 250 and 1000 h, both TCNi8 (thermodynamic) and MobNi4 (kinetic mobility) database were applied.

Results

As-Deposited Microstructure

The microstructure of the laser clad stellite 6 is shown in Fig. 1. The clad is ~ 1.2 mm thick and shows very good clad-substrate continuity. The elemental maps

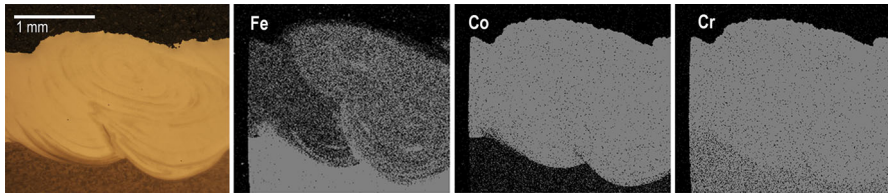


Fig. 1 Optical image and elemental maps on the cross section of the as-deposited laser clad showing non-uniform distribution of iron elements in the clad

of the clad in Fig. 1 indicate an inhomogeneous distribution of iron which stemmed from melting of the stainless steel substrate during cladding and subsequent iron dilution into the clad. The average amount of iron in the clad was 16 ± 2 wt% and it increased from ~ 14 wt% close to the surface to ~ 20 wt% in the vicinity of the clad/substrate interface. The clad shows a typical solidification microstructure with localized cells representing material flows due to the steep temperature gradient during cladding. No crack was present in the clad which is, in general, difficult to achieve in the hard facing alloys. The microstructure was also free from any defects (cracks or voids).

While analysis of the PXRD pattern of the as-deposited surface showed the presence of oxides (not shown here), after the grinding, which left a ~ 0.85 mm thick clad, only a mixture of fcc and hcp Co–Cr–Fe–W-rich solid solution and the minor presence of M_7C_3 type carbide were found (see Fig. 2 for phase identification of clad and coating PXRD patterns).

Figure 3 shows the BSE images of the HVOF thermal sprayed stellite 6 coating onto a 304 stainless steel substrate. The coating is around $250 \mu\text{m}$ thick, and it appears to be well bonded to the substrate without any cracks. The dark areas at the coating–substrate interface are embedded grit from the pre-deposition grit blasting operation. The microstructure of the coating is typical of the HVOF dense metallic coating with a low degree of porosity. HVOF thermal spraying using a liquid fuel tends to result in a relatively low amount of oxides in the coatings than in gas fuel HVOF [22]. Indeed, no oxides were detected by PXRD on the coating surface (not shown here). However, it should be noted that the detection limit for the given experimental set-up is in the vicinity of 1 wt%. The elemental composition determined from a $180 \times 180 \mu\text{m}$ area in the coating was as follows: Cr 29.3 ± 0.3 , Si 1.3 ± 0.1 , Fe 2.2 ± 0.1 , W 5.9 ± 0.3 , O 1.9 ± 0.3 , Co bal. (in wt%). This matches well with the composition of the feedstock powder. The phase composition was almost exclusively of fcc Co–Cr–W solid solution with the hcp structure accounting for 2–3 wt% according to QRR. After the top layer was ground off, the thickness of the coatings was $\sim 200 \mu\text{m}$ for the high-temperature corrosion tests.

Gas Phase Attack of the Samples

The scales that formed after 250 h exposure of the samples without deposits were poorly bonded to either the coating or the clad. The scales were discontinuous due to

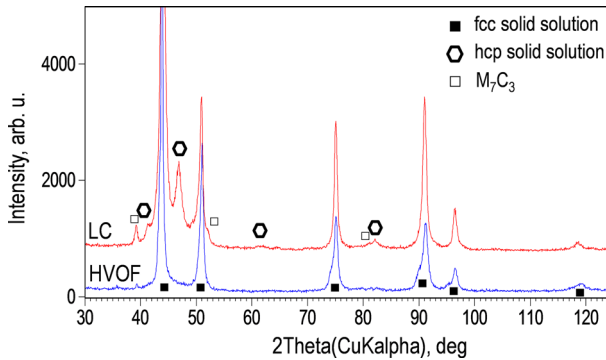


Fig. 2 PXRD patterns of laser clad (LC) and HVOF coating

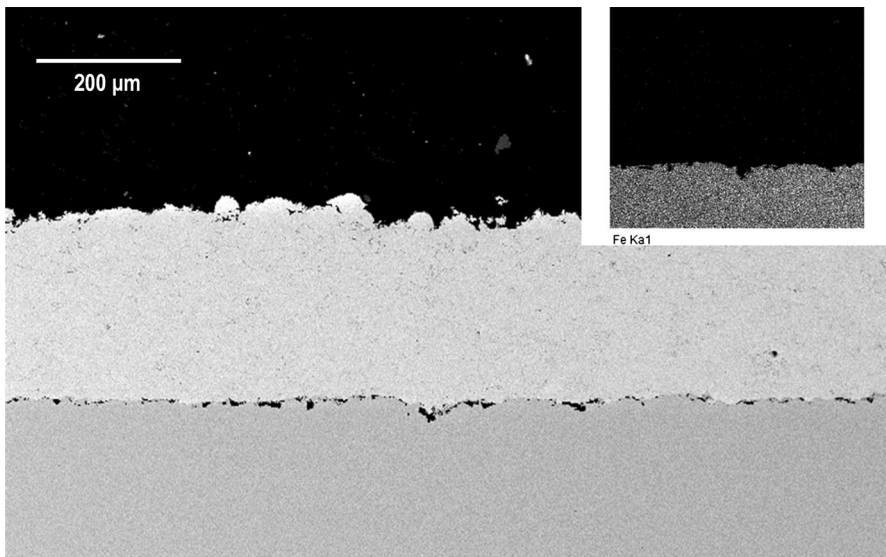


Fig. 3 BSE image of the HVOF stellite 6 coating, the dark areas on the interface are artefacts from grit-blasting by alumina. An elemental map of iron is displayed in the *inset*

localized spallation and their surface morphologies are shown in Fig. 4. While a fairly coherent layer of octahedral crystallites is present on the outermost surface of the scales on the HVOF coating (Fig. 4a, b), the occurrence of these octahedrons is seldom on the laser clad scale (Fig. 4c, d).

Figure 5 shows the elemental maps of the outermost surface of the HVOF coating after corrosion testing without a deposit. Areas for elemental mapping were chosen in such a manner that it would facilitate chemical analysis both on the scales and on the surface from which the scales spalled off. For the HVOF coating, the presence of chlorine was detected in the areas where spallation took place. There is significantly less cobalt on the scale surface as compared to the area without the scales. Chromium is present in higher concentration in the scale together with

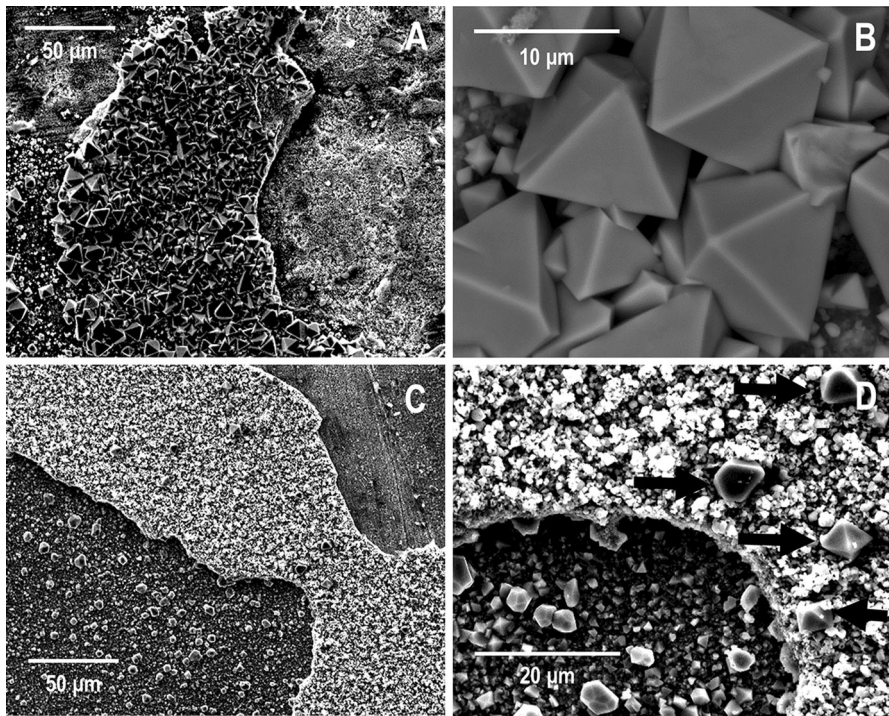


Fig. 4 Top surface morphology after 250 h of exposure without deposits revealing poor adhesion of the scales on **a** HVOF coating and **c** laser clad as well as the presence of octahedral crystals which were identified by PXRD as Co chromite spinels which are more abundant on **b** HVOF coating than on **d** laser clad

oxygen. The areas without the scale contain mostly cobalt, tungsten, chlorine with a small amount of chromium.

The irradiated volume during PXRD experiment encompassed both the scale and spalled areas. Rietveld analysis of the diffraction pattern in Fig. 6 can be used to determine phase composition of scales as dominantly composed of the cobalt chromite, i.e. CoCr_2O_4 with spinel structure, and chromite or Cr_2O_3 . The CoO was also identified, but only as a phase with minor presence. On the other hand, the fcc and hcp Co-rich phases come from the coating and the reflections corresponding to Cr_7C_3 and $\text{Co}_6\text{W}_6\text{C}$ suggest the presence of M_7C_3 and η type carbides on the coating–scale interface or in the exposed coating. For identification of the chlorine-containing phase, the literature sources [18] would analogously direct to $\text{CoCl}_2 \cdot 2\text{H}_2\text{O}$ for Co-based alloys, but both the positions of the weak and overlapping reflections and the subsequent Rietveld refinement gave significantly better results when hydrogenated HCl was considered. Although this phase shows a good match, the intensity is very low and significant overlap with other reflections do render this phase ambiguous. Due to the richness of crystalline phases present, only the final result of Rietveld refinement is presented with the positions of the

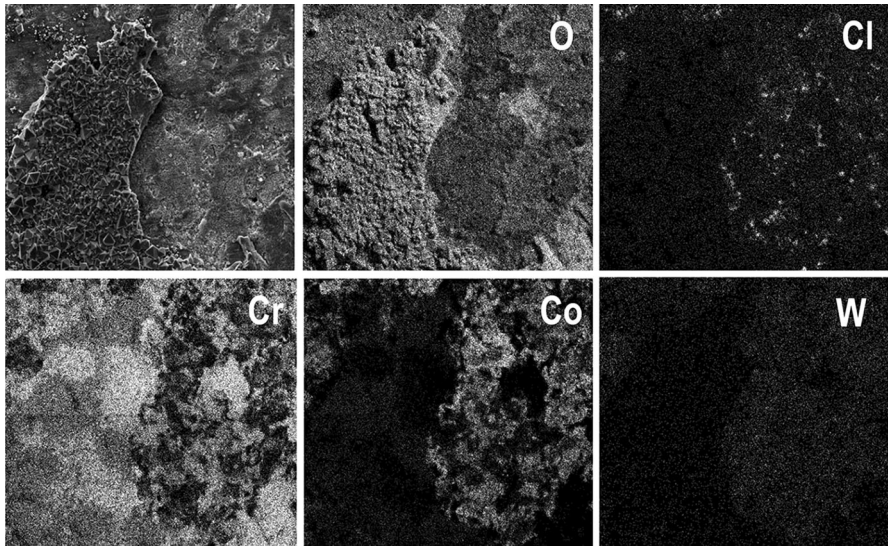


Fig. 5 Elemental maps as obtained by EDX on HVOF coating after 250-h exposure without deposit. The scale covers *left* half of the image, while on the *right*, the scale spalled off. Presence of chlorine element in the area where the coating spalled off is detected and amounted to ~ 1 wt.%

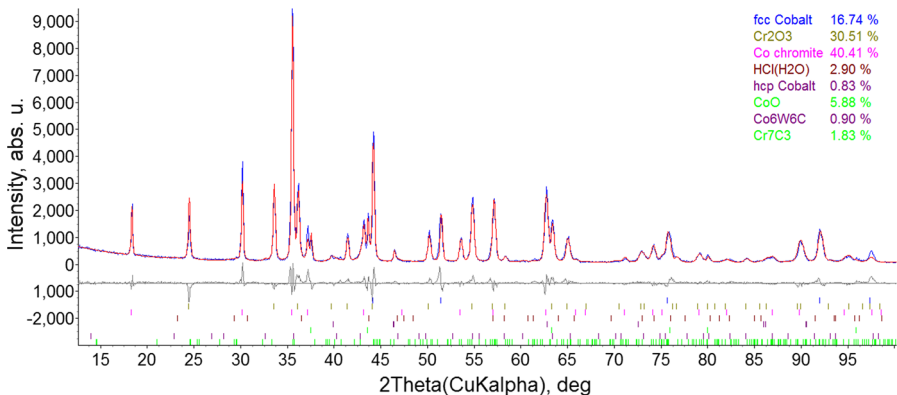


Fig. 6 Rietveld refinement of pattern measured on HVOF coating after 250-h exposure without deposit. Identified oxides in the scale, i.e. Cr₂O₃, CoCr₂O₄ and CoO, show reasonable fit of the measured data (in *blue*) by the model (in *red*). The *grey* curve at -800 intensity is the difference plot (Color figure online)

reflections of individual reflections from the phases matched by colour and sequence in the determined quantities in the top right corner of Fig. 6.

On the other hand, chlorine element was not detected in the EDX elemental maps on the laser clad sample after 250 h of exposure. Figure 7 also shows a chromium-rich oxide scale on the outermost surface and the areas where spallation occurred contain iron, cobalt and tungsten.

The XRD results of the laser clad sample is in Fig. 8. The reflections of the Co spinel are weaker and, consequently, its quantity determined by QRR is smaller.

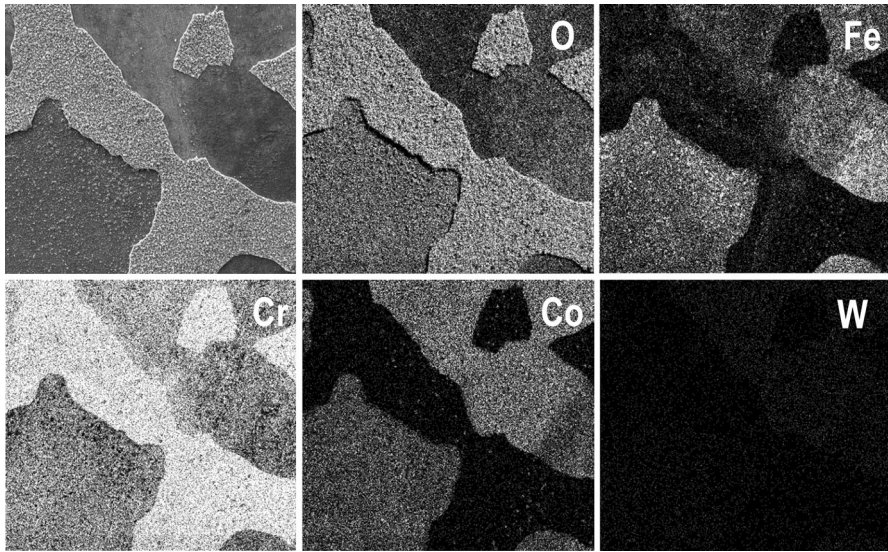


Fig. 7 Element maps as obtained by EDX on laser clad after 250-h exposure without deposit. Iron was detected on areas where the scale spalled off. Presence of chlorine atoms was below detection limit

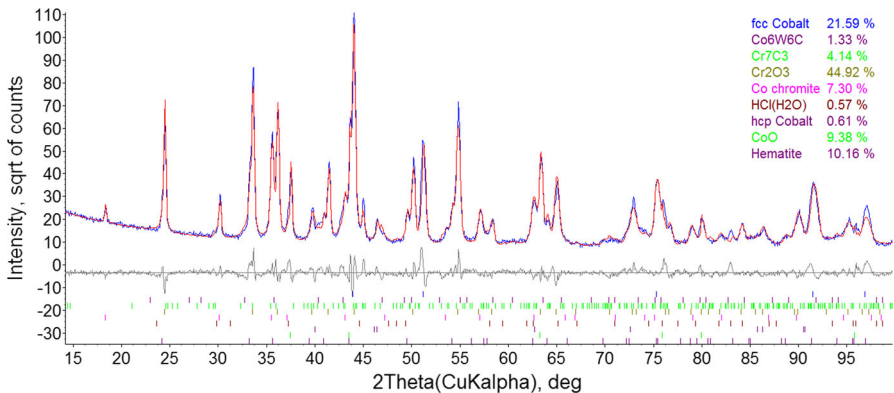


Fig. 8 Rietveld refinement of pattern measured on laser clad after 250-h exposure without deposit. The chlorine-containing phase is below the detection limit, but substantial amount of Fe_2O_3 (haematite) was found

Apart from the three same oxides detected on the surface of exposed HVOF coating, Fe_2O_3 (haematite) is detected. The presence of iron corresponds to the areas where spallation occurred (Fig. 7) and, thus, shows the dilution of the clad by iron from the substrate surface and the corresponding oxidation product. The presence of hydrogenated HCl was substantiated neither by EDX nor by PXRD, presumably because it is under detection limit of 1 wt%.

Rietveld refinement of the data provides not only feasibility of the phases presence based on the crystallographic information, but also the refined lattice

Table 1 Refined lattice parameters of three dominant oxides found in the scales compared with lattice parameters of pure materials [38-1479 for chromite, 22-1084 for Co chromite, 48-1719 for CoO]

Pattern	Co chromite (Å)	Cr ₂ O ₃ (Å)	CoO (Å)
HVOF	8.3837(4)	4.9670(4) 13.613(2)	4.1514(3)
Lase Clad	8.384(1)	4.9716(3) 13.613(1)	4.1536(3)
PDF-2	8.3299	4.9588 13.5942	4.2612

Estimated standard deviations are presented in brackets

parameters. These can be compared with the values for high purity phases and confronted with viability of substituting atoms, interstitials or vacancies in the lattice. Table 1 includes CoO lattice parameter and shows that CoO lattice in the coating and in the clad is by a significant 0.1 Å smaller compared to the database value. These calculations points to the presence of substoichiometric Co_{1-x}O rather than stoichiometric CoO. Analogically, Co chromite lattice is larger than for pure material, and since effective ionic radii or chromium ions are larger, the (Co,Cr)Cr₂O₄ is envisaged. Lattice parameters of chromia in the coating and clad are similar to those reported for pure Cr₂O₃.

Representative BSE images of polished cross sections of the laser clad and HVOF coating are shown in Fig. 9. Both the sample surfaces are covered with a layer of thin oxide scale. Thickness of the scale on the clad is 3.6 ± 0.7 μm, while the scale on the coating is 6.5 ± 0.7 μm. The oxide scale on the laser clad appears to split into two layers and the area marked by the arrow shows scale buckling and void between the layers. Spinel octahedra crystallites are well visible on the surface of the HVOF coating whose ~15 μm thick surface layer is corroded; however, the remaining coating was not attacked. The internal attack in the laser clad sample was around ~10 μm deep. The bright spots in the internal attack areas with sizes in low hundreds of nanometres are tungsten-rich and, thus, these were identified as η carbides. In the laser clad, the carbides were precipitated along the grain boundaries following the exposure. Correspondingly, mass-gain results after 250 h of exposure were 5.6 and 7.9 mg/cm² for the clad and the coating, respectively. It should be noted that this data include the mass gain of the substrate as well.

KCl-Deposit-Induced Corrosion

Figure 10 shows the BSE image of a polished cross section of the HVOF-sprayed coating which was covered with KCl deposit. The remaining coating thickness after 250 h exposure was around 160 μm. While the precipitation of tungsten-rich carbides was limited to a comparatively shallow layer of ~10 μm in HVOF coating without deposit, these are distributed virtually throughout the entire coating cross sections when the KCl deposit was on the surface. In addition, round shaped sub-micron porosity appeared within the splats, molten particles deformed and solidified on impact, which are labelled with yellow arrows. The top-hat-shaped splats

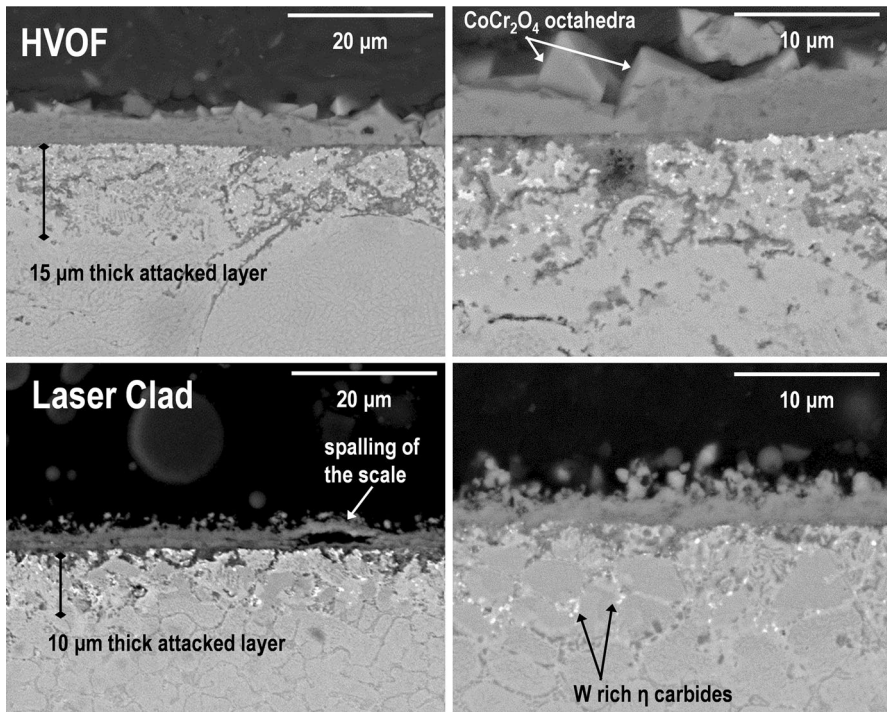


Fig. 9 BSE images of the cross section of HVOF coating and laser clad after 250-h exposure without deposit showing an oxide top layer with internal attack

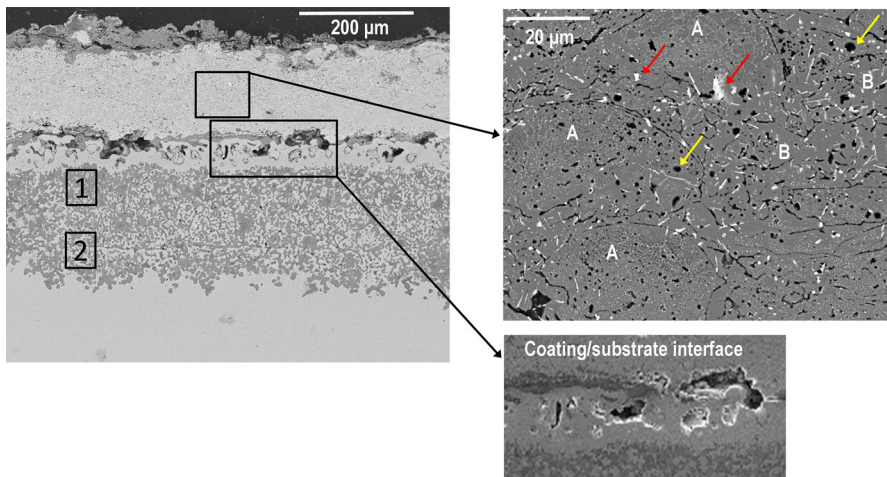


Fig. 10 BSE image of the HVOF-sprayed coating on SS304 substrate after exposure to KCl showing precipitation of tungsten-rich carbides in the entire coating thickness (red arrows) and presence of porosity (yellow arrow). Top-hat-shaped splats retained solid solution structure (A), but the part without the splat structure is completely Cr depleted (B). About 230 μm of SS substrate underneath the coating is attacked with voids created at the coating–substrate interface (Color figure online)

retained the solid solution microstructure from the as-sprayed coating, which are labelled A in the image, and the regions labelled B are completely depleted in chromium. Figure 10 also depicts the presence of voids at the coating–substrate interface and underneath the voids the substrate microstructure was attacked up to a thickness of $\sim 280\ \mu\text{m}$. The cavity formation has also been observed earlier by Evans [23] and Dravnieks and McDonald [24] that the internal oxidation occurred under the scale in the zone of consumption of the metal phase (also known as MCZ). EDX analysis performed in the $150 \times 150\ \mu\text{m}$ large area of the exposed coating showed only 1.0 wt% chromium, pointing to its severe depletion during the exposure. The chromium levels in the corroded substrate were 0.6 wt% in the area closer to the interface with coating (marked as 1 in Fig. 10) and 1.3 wt% in the area closer to the non-corroded material (area 2 in Fig. 10); 17.2 wt% of Cr was found in the non-corroded substrate of this sample.

The severity of chromium depletion is also confirmed by cross-sectional EDX elemental mapping in Fig. 11, where chromium in the coating is preserved only in the top areas of the splats with a top hat shape. The stainless steel substrate was also depleted in chromium up to a thickness of $\sim 280\ \mu\text{m}$. Moreover, the EDX maps reveal inward cobalt diffusion into the substrate up to $\sim 50\ \mu\text{m}$ and outward diffusion of iron from the substrate into the coating. Outward diffusion of chromium from both the substrate and the coating took place during the exposure, resulting in the depletion. A thin oxide scale is observed on the outermost surface of the coating which contains oxygen, cobalt and chlorine. Chlorine is also detected at the coating–substrate interface in the maps. It is interesting to note that oxygen was detected at the coating–substrate interface and within the substrate which suggests internal oxidation of the substrate. The mixed corrosion product (with oxides) on the coating had spalled during the test and what remained on the coating surface is a

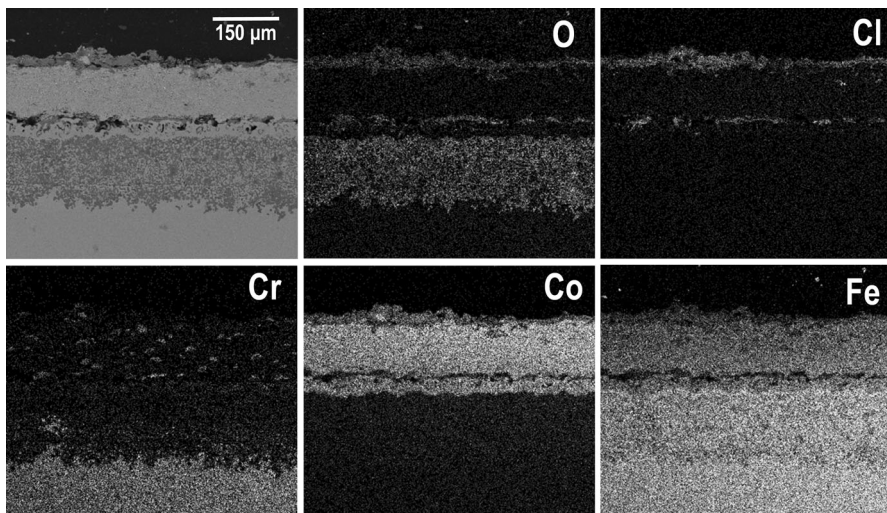


Fig. 11 EDX elemental maps of HVOF-sprayed coating exposed to KCl showing pronounced depletion of Cr in the whole coating and diffusion of Fe into it. Cobalt atoms diffused into the substrate

thin chlorine-rich phase. The PXRD analysis of the spalled pieces showed that the adjacent material to the coating was exclusively chromite, i.e. solely Cr_2O_3 reflections were observed in the diffraction pattern, while the patterns of the analysed three pieces from the top side showed presence of haematite and magnetite in approximate weight ratio of 9:1 (see phase identification in bottom, i.e. adjacent to coating, and top areas of the spalled piece in Fig. 12).

Nevertheless, the pattern in Fig. 13 was measured on the exposed coating after spallation of the corrosion/oxidation products and it shows, interestingly, presence of $\text{CoCl}_2 \cdot 2\text{H}_2\text{O}$ which is predicted by *active oxidation* theory. Moreover, there are two tungsten-rich phases, simple WC and CoWO_4 and no η carbide, even the small amount of silicon in the coating was oxidized to SiO_2 (quartz) and Co_3O_4 oxide was confirmed together with Cr_2O_3 .

Attack of the laser clad covered by KCl deposit was less severe, as can be seen in Fig. 13. The remaining thickness of the laser clad after the exposure was around

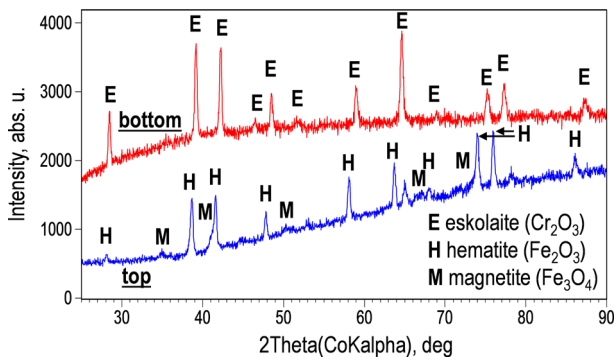


Fig. 12 Phase identification in patterns from representative corrosion deposit on HVOF coating that completely spalled off. *Bottom* pattern corresponds to surface adjacent to the coating, while the *top* pattern is from the outer free surface

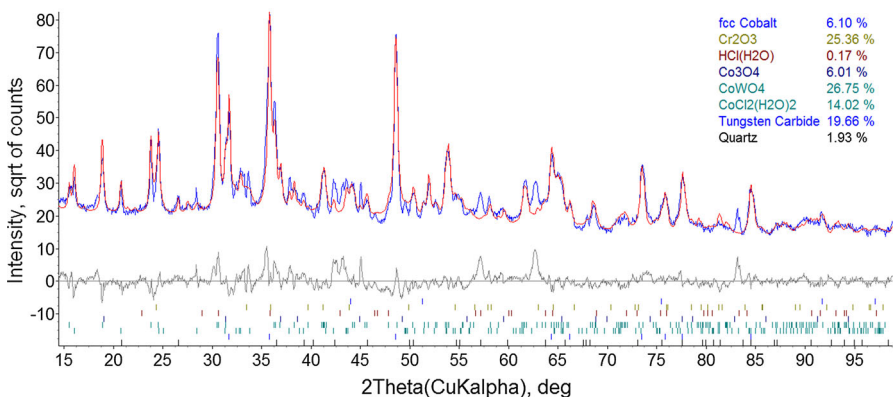


Fig. 13 Rietveld refinement of PXRD pattern from the HVOF coating (from which the scale during 250 h exposure with KCl deposit spalled off). There are two tungsten-rich phases of CoWO_4 and WC; Cl-rich $\text{CoCl}_2 \cdot 2\text{H}_2\text{O}$ phase has been unambiguously identified

1.2 mm. While the oxide layer on top of the clad was only $28 \pm 2 \mu\text{m}$ thick, beneath it, the clad exhibited internal attack up to a depth of $150 \mu\text{m}$, which also contained higher level of porosity. The scale has spalled in some areas, and a crack is present at the coating-scale interface (Fig. 14).

The line scan of selected elements (Fig. 15) confirmed up to $\sim 5 \text{ wt\%}$ chromium depletion from the top layer of $20 \mu\text{m}$, with depth further increasing, the Cr level is about 20 wt\% . The top $20 \mu\text{m}$ region of the coating also contains a higher level of Co (nearly $70\text{--}75 \text{ wt\%}$), which is in line with the depletion of chromium. The Fe content in the clad is due to dilution of the substrate as previously described in “As-Deposited Microstructure” section. There was no noticeable trend in tungsten content throughout the top region of the laser clad.

EDX elemental maps (Fig. 16) of the oxide layer on the top of the KCl-deposited clad shows a layered structure. On the very top, there is mainly an iron-rich oxide layer and the composition was detected to be FeO (wüstite) and Fe_3O_4 (magnetite) from the PXRD scans in Fig. 17. Underneath this iron-rich oxide, a layer of chromium-rich oxide is present, which was detected as Cr_2O_3 in the PXRD scan. There are some porosities present in the Cr_2O_3 layer in the coating. The scale also contains Co-based oxides and according to PXRD scans those are CoO, Co_3O_4 and CoWO_4 . Furthermore, Rietveld analysis of the sample surface showed the presence of 6 wt\% of K_3CrO_4 , which was not detected in the HVOF samples. While orthorhombic (space group *Pnma*) chromate phase of K_2CrO_4 was reported to originate in KCl induced corrosion of FeCrAl alloy [16], we detected potassium peroxochromate K_3CrO_4 which is tetragonal with space group *I*—42 m [25].

Discussion

Corrosion Behaviour of the Bare Surfaces

The scales developed on both the samples during the exposure suffered from spallation and were consequently not protective in nature. The scales formed on Co-

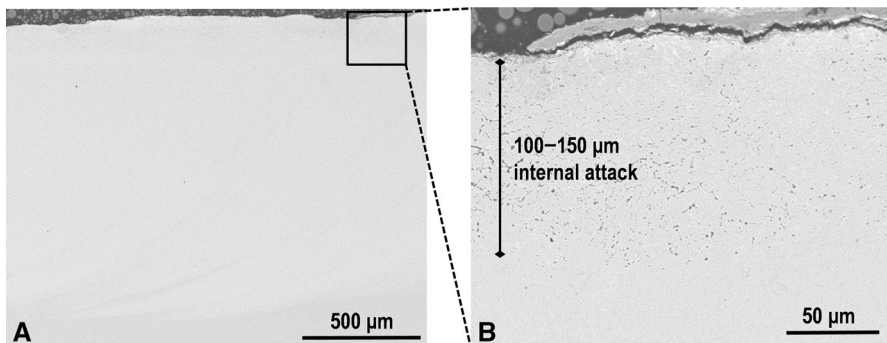


Fig. 14 BSE image of the laser clad sample after exposure to KCl deposit **a** showing the entire cross section and **b** high-magnification image showing $100\text{--}150 \mu\text{m}$ thick porous layer

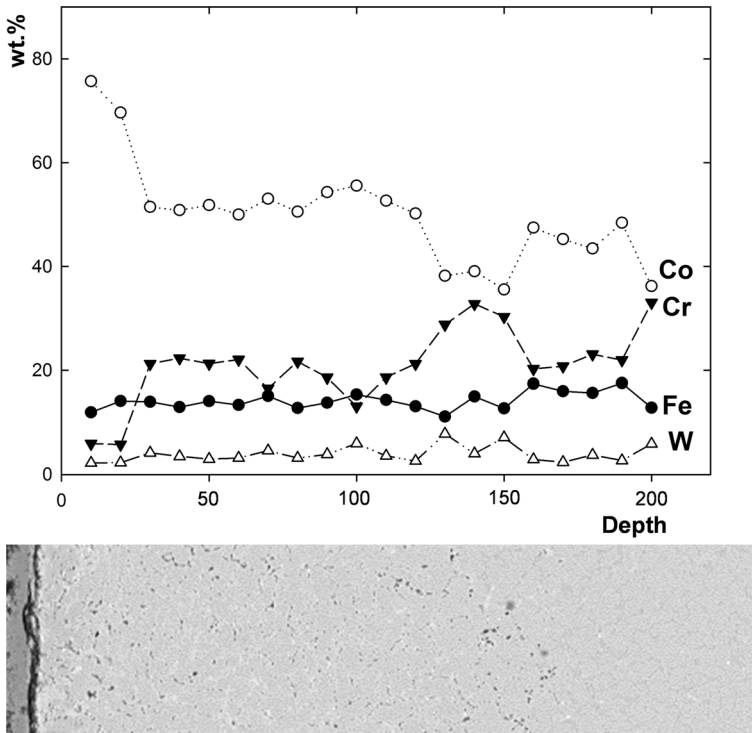


Fig. 15 Line scan through the top of the laser clad exposed to KCl deposit

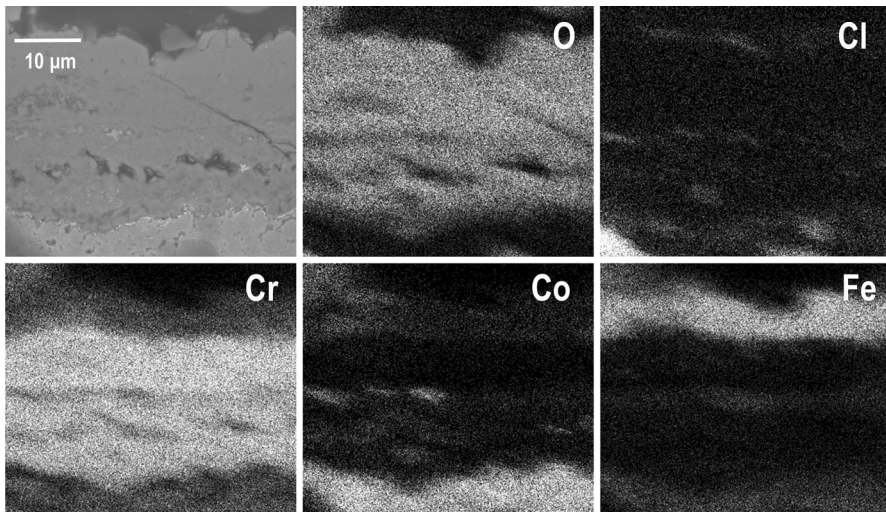


Fig. 16 Element maps as obtained by EDX on laser clad cross section after 250-h exposure with KCl deposit. Iron atoms are present in the bottom part (clad), but also on the top of chromium-rich oxide

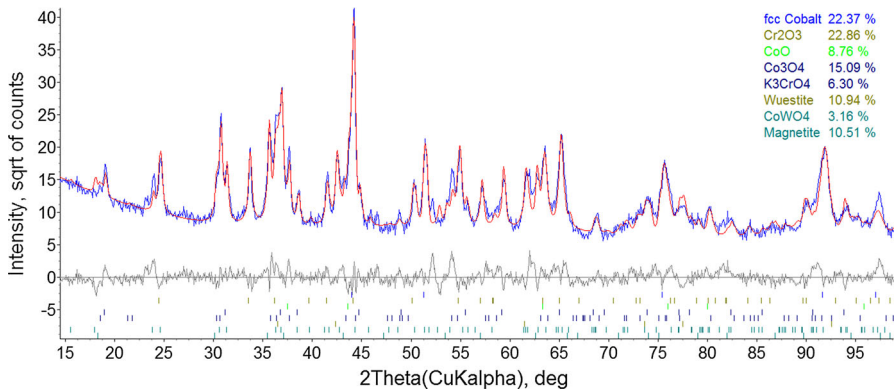


Fig. 17 Rietveld refinement of PXR D pattern from the laser clad sample after 250 h exposure with KCl deposit

based alloys exposed to oxidation environments have been reported to be prone to spallation. Stringer and Wright [26] attributed the spallation to poor adhesion of the cobaltous oxide scale to the metal surface due to the growth of oxide takes place at scale/gas interface rather than the scale/metal interface. According to Zahs et al. [18, 27], the worse adhesion of the scales in chlorine based environment is attributed to the existence of $\text{CoCl}_2 \cdot 2\text{H}_2\text{O}$ at the substrate–scale interface [23], but this phase was not found by XRD and hydrogenated HCl was the only viable chlorine-containing substance. There were three types of oxides identified on the surface of the exposed coating, i.e. CoO, Cr₂O₃ and (Co,Cr)Cr₂O₄. On the free surface of the scale, a layer of octahedral spinel crystallites was observed, the refined lattice parameter indicated that it is (Co,Cr)Cr₂O₄, because the pure CoCr₂O₄ spinel has smaller lattice parameter. Effective ionic radii for +2 and +3 states are (supposing low spin) 73 and 61.5 pm for chromium and 65 and 54.5 for cobalt, i.e. chromium ions are larger [28]. Since the (Co,Cr)Cr₂O₄ can be written as $(\text{Co}_{1-x}^{2+}\text{Cr}_x^{2+})\text{Cr}^{3+}\text{Cr}^{3+}\text{O}_4$, then lattice parameter of the cubic unit cell must be larger when compared with simple CoCr₂O₄ spinel. The same theory cannot be used for the lower value of CoO lattice that is of the rock salt structure. Defect structure of CoO has been well understood for a long time [29–31], which is a metal deficient, *p*-type electronic conductor, with $D(\text{Co})$ orders of magnitude greater than $D(\text{O})$. The amount of vacancies increase with rise in temperature [32, 33]. Mrowec and Przybylski [33] studied oxidation of pure cobalt in temperature range of 900–1300 °C and reported that a single-layer Co_{1-y}O scale grew according to parabolic kinetics with the process controlling the scale growth being outward diffusion of cation vacancies. The significantly smaller CoO lattice is in line with the defect metal deficient structure.

Now moving to the bulk microstructure, the HVOF coating during the 250 h exposure resulted in microstructural changes and phase transformation within the depth of ~15 μm. The precipitation of η carbides (Co₆W₆C) and M₇C₃-type carbides is observed only within the affected surface layer, thus, solely the temperature of 700 °C and the duration of 250 h is not sufficient for the carbide precipitation in the

coating and the depletions of chromium and cobalt ions were arguably the main factors leading to higher concentration of tungsten in the depleted zone and energetically favoured η carbide creation. The absence of tungsten outward diffusion was an expected phenomenon already described by Guyard et al. [34].

In contrast to the HVOF coating, the laser clad did not retain the same phase and elemental composition of the Co–Cr–W–C alloy and as a consequence of the dilution of iron into the entire clad, the exposed surface was rather a quinary system of Co–Cr–Fe–W–C. The most apparent difference between the scales on the coating and on the clad is the smaller thickness of the oxide layer and the absence of continuous Co spinel layer, with its crystals occurring only as solitary octahedra on chromia-rich scale. The XRD analysis also revealed the presence of Fe_2O_3 and even though the $\sim 3.5\ \mu\text{m}$ thickness scale did not facilitate precise Fe, Cr and Co mapping due to the pear-shaped interaction volume of the electron beam, the EDX indicated that Cr-rich oxides are on the top layer with Fe_2O_3 and CoO formation underneath. Even for the clad, the CoO has smaller lattice due to the presence of vacancies, the possibility of (Co,Fe)O phase indicated in Co–Fe systems [35] was rendered infeasible to be distinguished due to the small difference between the effective atomic radii of both iron and cobalt in +2 state. The Co chromite octahedra are of (Co,Cr) Cr_2O_4 type.

In order to better understand the selective oxidation behaviour of both HVOF and laser clad stellite 6 coatings at high temperatures, thermodynamic calculations were carried out using Thermo-Calc software with TCNi8 database. Figure 18a–c shows the thermodynamic calculations of the oxide scale formation on a stellite 6 coating (Co 28.3Cr 4.8W 2.2Ni 1.5Fe in wt%) as a dependency of oxygen partial pressure and at a constant temperature of 700 °C with different compositions of Fe: (a) 1.5 wt%; (b) 10 wt%; and (c) 15 wt%. We have earlier identified the presence of Fe in the as-received laser clad coating; and the Fe content in both coatings also increased due to the inter-diffusion with stainless steel substrate. Accordingly, these three compositions were chosen to study the effect of Fe content on the selective oxidation behaviour of coatings. The diagrams in Fig. 18 can be understood in this way: during oxidation, less stable oxides will form first on the alloy surface under high partial pressures of O_2 (on the right side of the plot). As the scale thickens, the partial pressure of O_2 gradually reduces, and more stable oxides will form underneath, which results in a multi-layered scale. From the calculation results in Fig. 18a, it indicates that the stable oxidation products at 700 °C will be CoCr_2O_4 (outer layer) and CoO (inner layer). If the content of Fe increases (See Fig. 18b, c), the growth of Fe_2O_3 will consume more CoO and form another spinel CoFe_2O_4 . The calculations agree well with the experimental results that the oxides on stellite 6 are consisted of an outer layer of spinel (CoCr_2O_4) and an inner layer of Halite (CoO). For laser clad coatings containing certain amount of Fe, the increase of Fe will promote the formation of Fe_2O_3 and even form another spinel CoFe_2O_4 .

Corrosion Behaviour of the Samples with KCl Deposit

KCl is a substance known to strongly accelerate corrosion of stainless steel and, therefore, protective overlay coatings are of significant interest for applications in

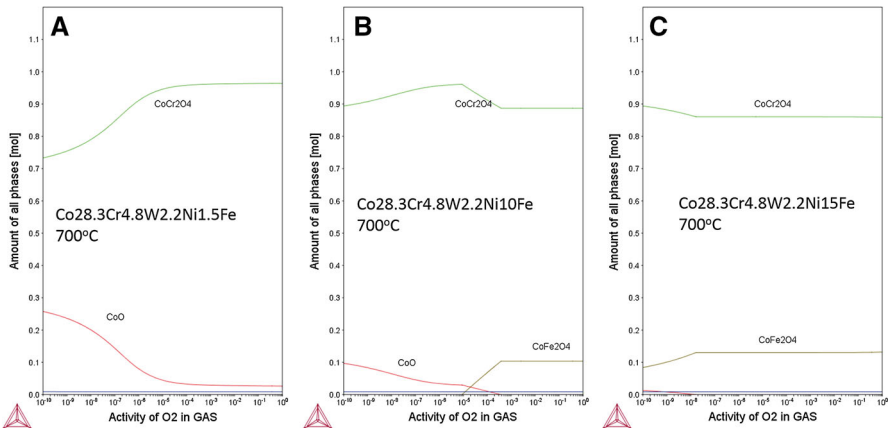


Fig. 18 Thermo-Calc calculations of oxide scale formations on a stellite 6 coating (Co 28.3Cr 4.8 W 2.2Ni 1.5Fe, wt%) as a dependency of oxygen partial pressure and at a constant temperature of 700 °C with different compositions of Fe: **a** 1.5 wt%; **b** 10 wt%; and **c** 15 wt% (the increase of Fe is at the expense of Co)

biomass fuel fired power plants. Pettersson et al. [36] reported that the acceleration is due to the protectivity loss when the chromia-rich scales are damaged by formation of chromate (K_2CrO_4). Effectively, the haematite layer with K_2CrO_4 rapidly grew outward while spinel (Fe,Cr,Ni)₃O₄ grew inward [37] and chlorine is released in gaseous form, presumably as HCl or Cl₂. Moreover, this degradation mechanism significantly accelerates with increased temperature [38].

Figures 10 and 14 illustrate marked difference in the corrosion of laser clad and the HVOF coating. Firstly, the layer with severe chromium depletion, i.e. to about 5 wt%, in the clad is 20 μm thick and in the deeper 150 μm the chromium level decreased from 26 (prior to exposure) to 20 wt%. Secondly, the main effects of the exposure on the microstructure of the clad are the emergence of porosity, which was confirmed by images in SE mode. The grains of tungsten-rich phase, which are CoWO₄ according to analysis of PXRD data, are observed only in the areas with severe chromium depletion of the clad. The outward growing layer rich in iron oxides is composed of wüstite and magnetite; however, since the Cr atoms were also detected (see Fig. 16), the magnetite is more likely (Fe,Cr)₃O₄. Underneath, 10-μm-thick chromia layer and further below, another Cr- and Co-rich oxide layer composed of substoichiometric CoO and Co₃O₄ phases was created. The lattice parameter of CoO is similar to those observed on bare surface exposure, and the lattice parameter of spinel Co₃O₄ has the expected value for pure phase. Even though there is a clear correspondence between occurrence of Co and Cl atoms in Fig. 16, the expected CoCl₂·2(H₂O) was not found by X-ray diffraction. On the other hand, we identified the potassium peroxochromate (K₃CrO₄) which is deemed responsible for the tenfold increase in oxide layer thickness in comparison with bare clad exposure, analogously to mechanism described in [36]. These results indicate that KCl is so aggressive that it significantly accelerates the corrosion rate by

rapidly consuming Cr with the formation of non-protective chromates, which therefore promotes the formation of other oxides (Fe & Co oxides).

HVOF coating covered with KCl is noted for the most severe corrosion attack. Not only is the entire coating porous and exhibits virtually uniform presence of tungsten-rich carbides, but the stainless steel substrate beneath was attacked as well, up to the depth of almost 280 μm . However, there are two notable observations from the viewpoint of diffusion. The chromium elemental map in Fig. 11 shows extreme and almost complete chromium depletion up to the depth of about 470 μm and, in fact, the only areas that were able to retain some chromium were those on the top of the hemispherical splats where the solid solution microstructure from the feedstock was preserved. There are several effects of the chromium depletion such as origination of porosity and voids together with tungsten-rich areas in the coating. Consequently, the coating became virtually transparent for oxygen which was able to diffuse through and attack the stainless steel substrate. The excess of tungsten led to creation of two tungsten-rich phases, WC and CoWO_4 . Moreover, even the 1.2 wt% of silicon in the stellite 6 was oxidized to SiO_2 . Outward diffusion of iron from the substrate into the coating and further into the oxide layer also took place with the iron atoms forming dominantly a haematite layer on the chromite, as shown by PXRD analysis of spalled corrosion products.

There can be some uncertainty about where the original coating–substrate interface lies on Figs. 10 and 11; the best indication would be the area with splats in Fig. 11. Hence, the prior coating–substrate interface is actually formed by substantial voids and the cobalt elemental maps illustrate inward cobalt diffusion into the steel substrate. The enormous fluxes during high-temperature diffusion lead us to certitude that the voids are actually Kirkendall voids by nature and the shift of interfacial line, which was described by Smigelskas and Kirkendall [39], support this statement. The interfacial line shift is documented in Fig. 11 by cobalt elemental map. Figure 19 shows the concentration profiles (in weight fraction) of Co, Fe, Cr, and Ni, on the cross sections of the diffusion couple of stellite 6 coatings (left) and 304 stainless steel (right) at 700 °C (973 K) simulated by using DICTRA for: (a) 0 h; (b) 250 h; and (c) 1000 h. The original coating–substrate interface at time = 0 in Fig. 19a is also marked in Fig. 19b, c when time = 250 and 1000 h. The simulations agree well with our experimental results that the inter-diffusion between coating and substrate caused the inwards diffusion of Co and Cr as well as the outwards diffusion of Fe. After 250-h and 1000-h treatment, the coating–substrate system nearly reached equilibrium that no severe inter-diffusion would occur. This result confirms that the depletion of Cr in Fig. 11 was not caused by the inwards diffusion of Cr towards the substrate. This could only be due to the rapid growth of non-protective chromate, which significantly consumed Cr and may even induce an outwards diffusion of Cr from the substrates. On the other hand, the depletion of Cr in the coating due to the rapid growth of chromate would also constantly break the equilibrium between the coatings and substrates. It will further promote the outwards diffusion of Fe, as well as the inwards diffusion of Co, resulting in a greater shift of the original coating–substrate interface and leading to the formation of other non-protective oxides, such as CoO , Fe_2O_3 and CoFe_2O_4 . Eventually, the anticipated chlorine-rich $\text{CoCl}_2 \cdot 2\text{H}_2\text{O}$ phase was found in large

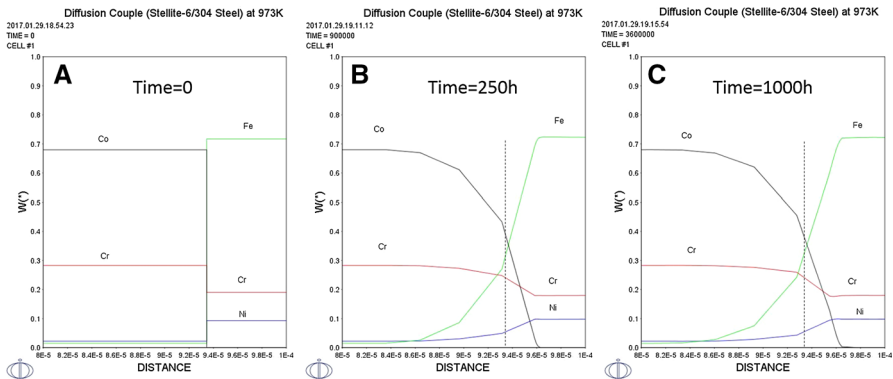


Fig. 19 DICTRA simulations: the concentration profiles (in weight fraction) of Co, Fe, Cr, and Ni on the cross sections of the diffusion couple of stellite 6 coatings (*left*) and 304 stainless steel (*right*) at 700 °C (973 K) for: **a** 0 h; **b** 250 h; and **c** 1000 h

quantities on the coating surface from which the corrosion layer completely spalled and, hence, the presence of $\text{CoCl}_2 \cdot 2\text{H}_2\text{O}$ further worsened the adhesion of oxide-rich layer to the HVOF coating.

Summary

A Co–Cr–W–C quaternary alloy stellite 6 was HVOF thermal sprayed and laser clad onto a 304 stainless steel substrate, and the coated samples were exposed for 250 h at 700 °C to atmosphere composed of 500 ppm of HCl, 5% oxygen and balance of nitrogen. The coatings and clads, which were either bare or were covered with KCl deposit, exhibited various extents of attack with discontinuous scales with poor spallation resistance. The following conclusions can be drawn from this study.

- The bare samples led to corrosion of 10 and 15 μm thick of clad and coating, respectively, which was manifested by precipitation of η carbides ($\text{Co}_6\text{W}_6\text{C}$) and M_7C_3 -type carbides together with increased porosity and chromium depletion from the solid solution. CoO with defect structure together with Cr_2O_3 and $(\text{Co,Cr})\text{Cr}_2\text{O}_4$ spinel oxides were formed on the top surface. Chlorine-rich phase, HCl (H_2O), was detected on the HVOF surface after the exposure. Dilution of iron atoms from the substrate into the laser clad during deposition resulted in a distinctive two-layer scale structure with the Fe_2O_3 layer being the inner layer and Cr_2O_3 the outer.
- The samples covered with KCl deposit resulted in accelerated corrosion attack of the clad and the coatings mainly via severe chromium depletion, $\sim 280 \mu\text{m}$ and $\sim 20 \mu\text{m}$ in HVOF and laser clad, respectively.
- The presence of KCl in laser clad altered the sequence of the oxide layers in the scale with FeO and Fe_3O_4 being the outer layer with chromia and chromia/ Co_3O_4 /vacancy-rich CoO being the inner layers. The presence of K_3CrO_4 resulted in accelerated corrosion manifested by increased porosity within the

100- to 150- μm -thick surface layer. Severe depletion onto 5 wt% in 20 μm thick layer is observed along with emergence of tungsten-rich areas of CoWO_4 .

- Splat-like microstructure of HVOF coating suffered from significant chromium depletion under the given conditions in KCl induced corrosion. Outward diffusion of chromium from both coating and 280- μm -thick layer of steel, outward diffusion of iron from the substrate through the coating to the metal-scale boundary as well as inward diffusion of cobalt from coating to the substrate led to Kirkendall voids at the coating–substrate interface. Overall chromium levels in the coating decreased from initial 29 to 1 wt.% effectively causing precipitation of WC and CoWO_4 in the entire coating. On the coating–scale interface, 10- μm -thick $\text{CoCl}_2 \cdot 2\text{H}_2\text{O}$ layer was formed and as a consequence the scales spalled off. While the scale surface adjacent to $\text{CoCl}_2 \cdot 2\text{H}_2\text{O}$ was purely of chromite composition, the top outer layer was composed of 9:1 $\text{Fe}_2\text{O}_3:\text{Fe}_3\text{O}_4$.

Acknowledgements This work was supported by the UK Engineering and Physical Sciences Research Council (EPSRC) project entitled Ultra-Supercritical (USC) steam power generation technology with Circulating Fluidized Bed (CFB): Combustion, Materials and Modelling (USC-CFB-CMM) (EP/M01536X/1). We appreciate support for this project from Uniper, UK and Foster Wheeler Energia, Finland. We also acknowledge Mr Rory Screaton at the University of Nottingham for the spray runs.

Open Access This article is distributed under the terms of the Creative Commons Attribution 4.0 International License (<http://creativecommons.org/licenses/by/4.0/>), which permits unrestricted use, distribution, and reproduction in any medium, provided you give appropriate credit to the original author(s) and the source, provide a link to the Creative Commons license, and indicate if changes were made.

References

1. K. C. Antony, *JOM Journal of the Minerals Metals and Materials Society* **35**, 52 (1983).
2. W. Betteridge, *Cobalt and Its Alloys*, (Wiley, Hoboken, 1982).
3. O. H. Wyatt and D. Dew-Hughes, *Metals, Ceramics and Polymers*, (Cambridge University Press, London, 1974).
4. J. L. De Mol Van Otterloo and J. T. M. De Hosson, *Acta Materialia* **45**, 1225 (1997).
5. H. Hack and G. S. Stanko, Update on fireside corrosion resistance of advanced materials for ultra-supercritical coal-fired power plants, in *The 31st International Technical Conference on Coal Utilization & Fuel Systems*, 2006, pp. 21–25.
6. M. X. Yao, J. B. C. Wu and Y. Xie, *Materials Science and Engineering A* **407**, 234 (2005).
7. W. Hume-Rothery, R. E. Smallman and C. W. Haworth, *The Structure of Metals and Alloys*, 5th ed, (The Institute of Metals, London, 1988).
8. Q. Y. Hou, J. S. Gao and F. Zhou, *Surface & Coatings Technology* **194**, 238 (2005).
9. S. Houdkova, E. Smazalova and Z. Pala, *Journal of Thermal Spray Technology* **25**, 546 (2016).
10. A. Hjørnhede, P. Sotkovszki and A. Nylund, *Materials and Corrosion* **57**, 307 (2006).
11. T. S. Sidhu, S. Prakash and R. D. Agrawal, *Surface & Coatings Technology* **201**, 1602 (2006).
12. Z. Česánek, J. Schubert, Š. Houdková, O. Bláhová, and M. Prantnerová, in *Key Engineering Materials*, vol. 662 (2015), pp. 115–118.
13. F. R. Morral, *Corrosion* **25**, 307 (1969).
14. P. K. Kofstad and Z. Hed, *Journal of the Electrochemical Society* **115**, C232 (1968).

15. C. A. Phalnikar, E. B. Evans and W. M. Baldwin, *Journal of the Electrochemical Society* **103**, 429 (1956).
16. N. Israelsson, J. Engkvist, K. Hellström, M. Halvarsson, J.-E. Svensson and L.-G. Johansson, *Oxidation of Metals* **83**, 29 (2015).
17. N. Israelsson, K. A. Unocic, K. Hellström, T. Jonsson, M. Norell, J.-E. Svensson and L.-G. Johansson, *Oxidation of Metals* **84**, 105 (2015).
18. A. Zahs, M. Spiegel and H. J. Grabke, *Corrosion Science* **42**, 1093 (2000).
19. T. Hussain, N. J. Simms, J. R. Nicholls and J. E. Oakey, *Surface & Coatings Technology* **268**, 165 (2015).
20. H. M. Rietveld, *Acta Crystallographica* **22**, 151 (1967).
21. J.-O. Andersson, T. Helander, L. Höglund, P. Shi and B. Sundman, *Calphad* **26**, 273 (2002).
22. B. Song, Z. Pala, K. T. Voisey, and T. Hussain, *Surface & Coatings Technology* (2016). doi:[10.1016/j.surfcoat.2016.07.046](https://doi.org/10.1016/j.surfcoat.2016.07.046)
23. H. E. Evans, *Materials Science and Technology* **4**, 1089 (1988).
24. A. Dravnieks and H. J. McDONALD, *Journal of the Electrochemical Society* **94**, 139 (1948).
25. R. Stomberg, *Acta Chemica Scandinavica* **17**, 1563 (1963).
26. J. Stringer and I. G. Wright, *Oxidation of Metals* **5**, 59 (1972).
27. S. Chevalier, S. Ched'Homme, A. Bekaddour, K. Amilain-Basset and L. Buisson, *Materials and Corrosion* **58**, 254 (2007).
28. N. N. Greenwood and A. Earnshaw, *Chemistry of the Elements*, 2nd edn. (Butterworth-Heinemann, Oxford, 1997).
29. J. S. Sheasby and B. Gleeson, *Oxidation of Metals* **32**, 379 (1989).
30. A. Atkinson, *Reviews of Modern Physics* **57**, 437 (1985).
31. P. Kofstad, *Nonstoichiometry, Diffusion, and Electrical Conductivity in Binary Metal Oxides*, vol. 155, (Wiley-Interscience, New York, 1972).
32. H. N. Ok and J. G. Mullen, *Physical Review* **168**, 550 (1968).
33. S. Mrowec and K. Przybylski, *Oxidation of Metals* **11**, 365 (1977).
34. C. Guyard, A. Barbangelo, C. H. Allibert and J. Driole, *Journal Materials Science* **16**, 604 (1981).
35. P. Mayer and W. W. Smeltzer, *Journal of the Electrochemical Society* **121**, 538 (1974).
36. J. Pettersson, H. Asteman, J.-E. Svensson and L.-G. Johansson, *Oxidation of Metals* **64**, 23 (2005).
37. T. Jonsson, J. Froitzheim, J. Pettersson, J.-E. Svensson, L.-G. Johansson and M. Halvarsson, *Oxidation of Metals* **72**, 213 (2009).
38. J. Pettersson, J.-E. Svensson and L.-G. Johansson, *Oxidation of Metals* **72**, 159 (2009).
39. A. D. Smigelskas and E. O. Kirkendall, *Transactions of AIME* **171**, 130 (1947).